This is a repository copy of *Effect of mesogenic corona on type and anisotropy of gold nanoparticle superlattice: when can tail wag the dog?*.

White Rose Research Online URL for this paper:
https://eprints.whiterose.ac.uk/195794/

Version: Published Version

Article:

Zhao, Y., Li, Y.-X., Cao, Y. et al. (3 more authors) (2023) Effect of mesogenic corona on type and anisotropy of gold nanoparticle superlattice: when can tail wag the dog? Chemistry – A European Journal, 29 (11). e202203673. ISSN 0947-6539

https://doi.org/10.1002/chem.202203673

The Effect of Mesogenic Coronas on the Type and Anisotropy of Gold Nanoparticle Superlattices: When Can the Tail Wag the Dog?

Yang-yang Zhao,[a] Yaxin Li,[b] Yu Cao,[a] Georg H. Mehl,*[a, c] Feng Liu,*[a] and Goran Ungar*[a, d]

Abstract: The correlation between the size of nanoparticles, the structure and shape of mesogenic ligands and the ensuing assembly behaviour is not really understood. Closer inspection shows very surprising features. Here, 2- and 4-nm gold nanoparticles (NPs) were synthesized, and grafted with a forked ligand containing two rod-like mesogens in its branches: one cholesterol, the other with azobenzene. The 4-nm NPs also contained *n*-hexylthiol as co-ligand. They were found to form a FCC cubic superlattice, whereas the 2-nm NPs form hexagonal HCP with weak birefringence, hence with partially oriented ligands. The structures were compared with those of related systems containing a range of different azobenzene-to-cholesterol ratios, all giving body-centred tetragonal superlattices with various degrees of anisotropy. Geometric analysis is presented in terms of the asphericity of the NPs' surroundings, requirement for space-filling and structural anisotropy. Some general rules are derived to help design the soft corona around the NPs in order to obtain superlattices with the desired structure and anisotropy.

Introduction

Ordered gold and silver nanoparticles (NPs) have received much attention owing to their plasmonic resonance properties of interest for different applications such as memory devices,[1] polarized light emission[2] and metamaterials for super-lenses and possibly even visible-light negative refractive index materials leading to invisibility cloaks.[3] For some applications it is

[a] Y.-y. Zhao, Dr. Y. Cao, Prof. G. H. Mehl, Prof. F. Liu, Prof. G. Ungar
    Shaanxi International Research Center for Soft Matter
    State Key Laboratory for Mechanical Behaviour of Materials
    Xi'an Jiaotong University, Xi An Shi, Xi'an 710049 (P. R. China)
    E-mail: feng.liu@xjtu.edu.cn

[b] Dr. Y. Li
    School of Chemistry and Chemical Engineering
    Henan University of Technology
    Zhengzhou 450001 (P. R. China)

[c] Prof. G. H. Mehl
    Department of Chemistry, University of Hull
    Hull, HU6 7RX (UK)
    E-mail: g.h.mehl@hull.ac.uk

[d] Prof. G. Ungar
    Department of Materials Science and Engineering
    University of Sheffield
    Sheffield, S1 3JD (UK)
    E-mail: g.ungar@sheffield.ac.uk

    Supporting information for this article is available on the WWW under
    https://doi.org/10.1002/chem.202203673

necessary to arrange the particles in regular arrays, with either 2D or 3D order.[4] The nanoparticles could be functionalized with polymers,[5] covalently bound synthetic organic molecules[6] or biomolecules.[7] A number of studies focused on gold nanoparticles (AuNP) tethered with various hydrocarbon chain thiols of different length.[6a,8] With such simple ligands, the ratio between core size to ligand chain length is the dominant factor governing the type of superlattice.[6a,8a,c] In some cases where the gold core has uniform and well-defined polyhedral shape and size, such shapes also affects the overall packing.[9] Preparation methods like solvent evaporation,[5c] solvent vapour annealing,[10] annealing at elevated temperature,[11] or controlling reduction speed[12] have different efficiencies in developing an ordered structure. In some cases changing preparation methods can also lead to a different polymorphs.[6c] Studies by transmission electron microscopy (TEM) or scanning probe microscopy have shown that deposition on different substrates can also have an effect.[13] Most of the systems of NPs grafted with linear chains were precipitated from solution and studied by TEM, while structure formation in the bulk of these systems is often hampered by their glassy nature when dry. In systems of particles of a single type, by far the most common super-structures are face-centred cubic (FCC)[5a,c,6c,14] hexagonal close packing (HCP)[5a,6c,15] and, with long grafted chains, body-centred cubic (BCC)/body-centred tetragonal (BCT),[5c,8c,11,14] or the even more densely packed hexagonal Frank–Kasper C14 phase.[8c,16]

Attaching mesogenic (liquid-crystal-forming) ligands to a NP surface provides an opportunity to broaden the range of packing modes.[17] Highly anisotropic string-like arrays of AuNPs on an ordered hexagonal lattice have been obtained by attaching rod-like mesogenic ligands side-on (lateral attachment) to the NP surface through a flexible spacer, while at the

Chemistry–A European Journal

Research Article
doi.org/10.1002/chem.202203673

Chemistry
Europe
European Chemical
Societies Publishing

same time "diluting" the mesogenic corona with non-mesogenic alkylthiol "co-ligands".[17h,18] As the mesogens provided the column sheath and the co-ligand aggregated between the AuNPs, by changing the length and number of co-ligands the interparticle gap could be controlled.[18] When a cholesterol mesogen was used a chiral columnar structure was obtained, adding the possibility of combining circular dichroism and circular birefringence with plasmonic resonance effects.[17e]

Regarding isotropic and nearly isotropic phases of mesogen-coated AuNPs, in an early work, using an AB_2 benzyl ether dendron linked to the AuNP through a thioalkyl spacer, produced a BCC phase.[17a] In the approach by Kanie et al., a two-shell dendritic corona was attached to 7-nm AuNPs, the inner layer consisting of linear thioalkane to some of which a fairly large G2 dendron was attached forming the outer corona.[17c] This formed a simple cubic lattice, with only one particle per unit cell. Simple cubic packing of spheres is very inefficient in filling space but the successful design of dendron filling the large cubic interstice illustrates the power of bespoke mesogenic tailoring. Interestingly, in the case of the two-shell dendron-grafted AuNPs that gave the simple cubic, an unusual metastable columnar phase was found containing two kinds of columns, those densely and those sparsely populated with AuNPs.[17c] Another example of unusual lattices is the low-symmetry $P2_1 3$ cubic, effectively a distorted FCC, was obtained by grafting a different dendron to CdS quantum dots.[19]

Attaching rod-like mesogens side-on to the AuNP has produced not only anisotropic columnar structures but also isotropic and nearly isotropic ones. Thus attaching relatively short (3-ring) mesogens side-on to 2-nm AuNPs without any co-ligands gave a simple 3D hexagonal $P6/mmm$ lattice with undetectable birefringence.[18] However, diluting the soft corona with hexylthiol co-ligands produced the above-mentioned highly anisotropic columnar structure, but diluting it further by the longer dodecylthiol co-ligands resulted in a fully isotropic FCC structure. Thus, the nematogenic tendency of the short diluted rod-like mesogens was insufficient to impose anisotropy to the system of spherical NPs.

An intermediate case was observed when the shorter three-ring mesogen was "less diluted" by a somewhat smaller amount of $C_{12}H_{25}SH$ co-ligand. Under these conditions a novel 3D phase was obtained, space group $P6_3/mmc$.[20] The mesophase has hexagonal symmetry and is birefringent, but the nanoparticles have tetrahedral coordination. Its structure is in fact that of Bernal ice, ignoring hydrogens and with the oxygen atoms replaced by the NPs. The structure can be compared to the HCP, with which it shares the space group. However, where HCP has a single NP, this ice structure has two, one above the other along c. Given their low volume fraction, the particles are rather closely spaced, significantly closer than in the FCC or HCP structures. The resulting high interparticle interaction, plus the anisotropy of the structure and of mesogen orientation, were responsible for the large anisotropy of the plasmonic resonance shift.

In order to fill space around NPs it is advantageous for the ligands to have a divergent shape. Dendrons[17a,c,21] provide one solution, side-on attached straight[18,20] or bent rods.[17b] The third type that has been used and that is adopted in this work are forked bi-mesogenic Y-shaped ligands, with two mesogens branching off at the end of a spacer.[17h] The fourth way is attaching a bent rod-like mesogen end-on through a spacer.[17b,f,g,22] When straight-rod mesogens are attached end-on, usually only smectic phases are observed, sometimes modulated (plane group $c2mm$), but occasionally also cubic.[17b,f,g,22]
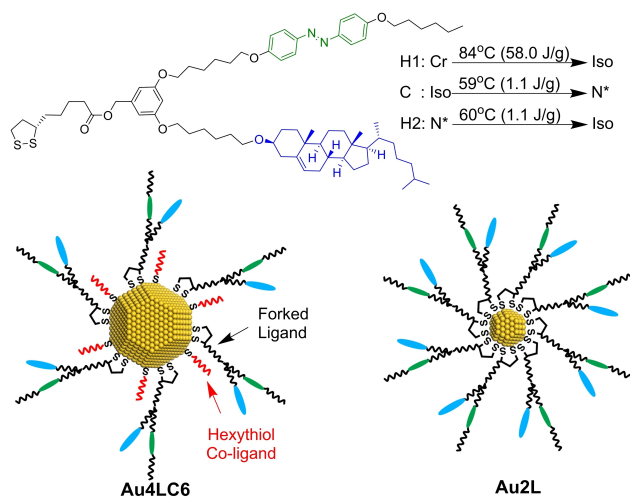
In our previous work,[17h] we adopted a type of forked ligand with a lipoic acid spacer carrying two rod-like mesogens, either both cholesterol (**C**) or one of them azobenzene (**A**). The **A** branch enabled induction of an order-disorder transition through photoisomerization with UV and visible light. The nanoparticles were found to assemble in a 3D BCT array whose interparticle distance was adjustable in 2D (x-y plane) thus allowing the anisotropic plasmonic effect to be tuned by changing the number of grafted forked ligands, that is, the ligand/co-ligand ratio. At the same time and independently Lawandosvski Wiktor et al. studied the structure of NPs decorated with bent-shaped mesogens end-on attached through a long flexible spacer, also containing dodecylthiol as co-ligand. On heating it showed a BCT-BCC-FCC phase sequence.[17g]

In this work we study two systems, one with AuNPs of 4-nm diameter and the other of 2-nm. The former has the forked mesogens **L** diluted by co-ligands, whereas the latter contains undiluted mesogens. The superlattices these systems develop are FCC and HCP, respectively. Electron density maps reveal strong anisotropy in positional disorder of NPs in the HCP, but not in the FCC. We compare the new results with those reported earlier to obtain a better understanding of AuNP self-assembly. We explored geometrical requirements that the soft ligands must satisfy for the hard metal NPs to form different isotropic (FCC, BCC) and anisotropic lattices (BCT, HCP). Metaphorically, we discuss the conditions under which the tail could wag the dog. Among other things we conclude that without the assumption of ligand migration on the AuNP surface the general trends observed would be difficult to explain.

Results

The two systems synthesized, with AuNPs of 4 and 2 nm in diameter bearing the forked mesogenic ligand **L** are shown in Scheme 1. **L** is the homologue of the ligands studied before,[17h] containing both a photoisomerizable azobenzene group and a chiral cholesterol group in the two branches. The synthesis of **L** and its LC properties are described in the Experimental Section and Sections S1.2 and S2.1 in the Supporting Information. Based on polarized optical microscopy (POM), differential scanning calorimetry (DSC) and small-angle X-ray scattering (SAXS), ligand **L** forms a chiral nematic (N*) phase at room temperature with the isotropic→N* transition at 60 °C on cooling (Figures S3 and S4). Its photoisomerization properties were studied by UV-vis spectroscopy, POM and ^{1}H NMR (Figures S5–S7).

Chemistry–A European Journal

Research Article
doi.org/10.1002/chem.202203673

Chemistry Europe
European Chemical
Societies Publishing

Scheme 1. Top: Molecular structure of the forked mesogenic ligand **L**. Bottom: Schematic representations of the two **L**-coated types of AuNPs— left: 4 nm and right: 2 nm.

In Figure 1, we show transmission POM of a contact preparation of ligand **L** (bottom right) and pentyl cyanobiphenyl (5CB), a typical nonchiral nematic (top left). 5CB area is black as the alignment is homeotropic, with the director (mean molecular axis) normal to the glass surface. The area of pure **L** (bottom right) is also black although here the molecules lie *in* the glass plane, but the helical axis, hence optic axis, is again normal to the substrate. The progression of colours is due to the removal from the white spectrum of "selectively reflected", that is, back-diffracted, light of increasing wavelength (purple to red) as the cholesteric pitch lengthens on going from pure ligand toward pure 5CB. Interesting paisley-like chiral fringes are seen at the boundary between the planar anchored (parallel to the glass) molecules in the colourful mixture and pure, or nearly entirely homeotropic 5CB.

Ligand **L** was attached to two gold nanoparticle types, with diameters ~2 and ~4 nm. Details of the NP synthesis are given in the Experimental Section and in Sections 1.3, 1.4 and 2.2 in
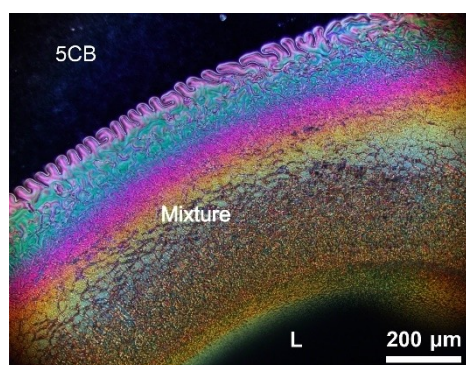
the Supporting Information. The size of **L**-coated ~2 nm AuNPs **Au2L**, as determined by TEM, was 2.05 ± 0.20 nm, where the quoted error is the standard deviation (Figure 2b). The size of the 4 nm AuNPs **Au4LC6** (Figure 2a) was found to be similar to that of dodecyl amine-decorated primary AuNPs (Figure S2) as determined by TEM. The size of the gold core was 4.10 ± 0.48 nm. The absence of free ligand in **Au4LC6** was confirmed by the fact that all NMR peaks were broad, as expected for a low mobility bound ligand (Figure S8). The surface density of the ligands was determined as ~4.7 ligands/nm^2 for both AuNPs based on TGA (Figure S9)/TEM/NMR analysis (Table S1). This value is slightly lower than that for systems using thiol as the linking group.[17f] This is attributed to the larger volume required by the disulfide link compared to that of the thiol.

The superlattice of the LC-AuNPs was investigated by SAXS. For **Au2L**, six Bragg peaks were observed at room temperature (Figure 3a), superimposed on a background containing two broad maxima, similar to the SAXS curve of the disordered isotropic melt shown in Figure S10a. In Figure 3a the experimental SAXS curve is shown together with the resolved Bragg components, the background and their sum. The SAXS Bragg peaks were indexed on a 3D hexagonal lattice, with the systematic extinctions consistent with the $P6_3/mmc$ space group and the hexagonal close-packed lattice. The observed and calculated d-spacings are listed in Table S2. The unit cell parameters are $a = 5.8$ and $c = 9.45$ nm, with $c/a = (8/3)^{1/2} = 1.63$, as expected from HCP packing of spheres.

The SAXS curve for **Au4LC6**, together with its resolved Bragg components is shown in Figure 3b, while that for isotropic melt is displayed in Figure S10b. The Bragg peaks are
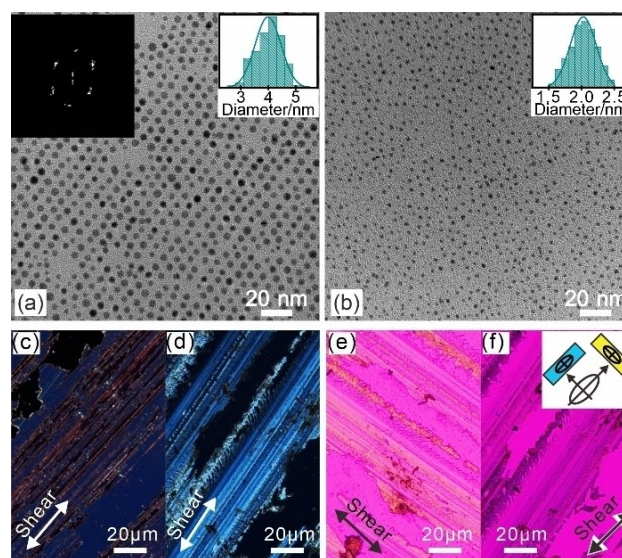

Figure 1. Room-temperature POM image of a contact preparation with ligand **L** at bottom right and 5CB at top left, with a concentration gradient in between after white light illumination. The colourful texture is a result of the increasing helical pitch of the N* phase formed by ligand **L**.


Figure 2. TEM images of nanoparticles a) **Au4LC6** and b) **Au2L**. The insets top right show the size distribution, and that at top left in (a) is the Fourier transform of the image. Optical micrographs between crossed polarizers (POM) of c) **Au4LC6** and d) **Au2L** sheared on a glass slide. e), f) Optical micrographs of sheared **Au2L** taken with crossed polarizers and an added λ-plate. The direction of the shear is indicated by a double arrow. The inset in (e) shows the index ellipses of the λ-plate (white) and the oriented domains in (e) (yellow) and (f) (blue).
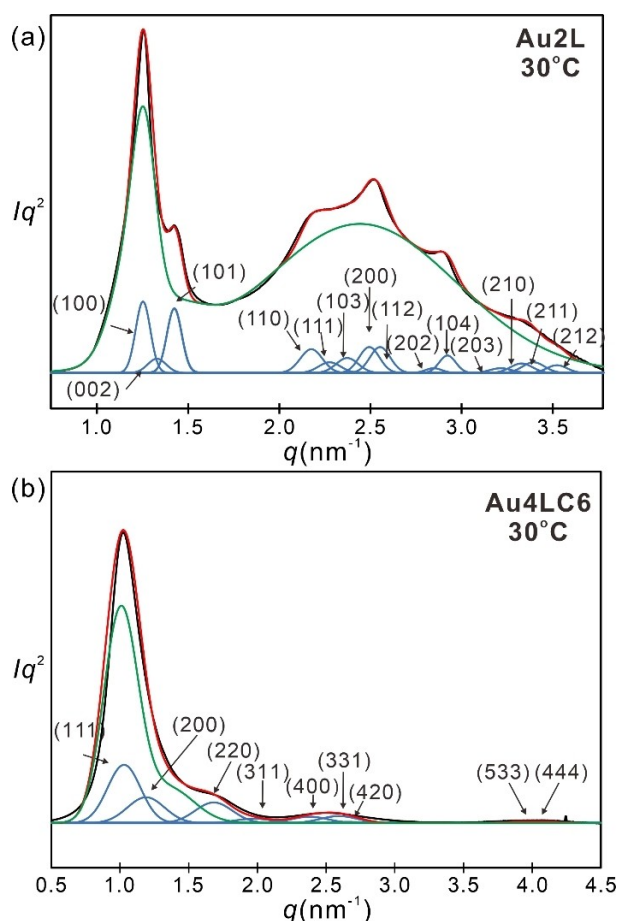
Figure 3. Transmission SAXS curves of unoriented LC-AuNPs with different sizes. a) **Au2L** at room temperature; b) **Au4LC6** at room temperature. Experimental: black, resolved components: blue, sum of components: red, amorphous: green.

approximately hexagonal lattice (Figure 2a). In contrast, a disordered monolayer is seen in **Au2L** (Figure 2b). The insets at the top right in both images show the size distribution histograms, and the inset in Figure 2a shows the Fourier transform of the image.

Shear-aligned LC-AuNPs samples were also studied by POM. The absence of birefringence in **Au4LC6** (Figure 2c) means that the mesogens in the FCC phase have no preferred global orientation, hence the structure can be regarded as isotropic. By contrast, the visible birefringence in Figure 2d means the mesogens in the HCP phase of **Au2L** have a degree of preferred orientation, that is, a degree of nematic character. The yellow and bluish streaks superimposed on the magenta background in POM images of the sheared **Au2L** with a λ-plate in Figure 2e and f, respectively, show that the slow axis, that is, the mesogen long axis, is oriented preferentially along shear direction.

The quality of the recorded SAXS data allowed reconstruction of electron density (ED) maps of the mesophases. The 3D maps are shown in Figure 4a, c, d, e. The procedure and choice of phases is described in the Supporting Information, including Figure S12. The high electron density regions (enclosed within green spheres in the maps) represent the gold nanoparticles. The prolate ellipsoids in the map of the HCP phase (Figure 4a, c) are due to an anisotropic Debye-Waller factor, similar to the "ellipsoids of vibration" of atoms in crystal structure representations. Therefore, the AuNP are positionally disordered preferentially along the c-axis, as schematically depicted in Figure 4b.

considerably broader compared with those for **Au2L**. The structure was indexed as FCC, space group $Fm\bar{3}m$. The observed and calculated d-spacings are listed in Table S3. The unit cell parameter is $a = 10.56$ nm. For both LC-AuNPs, no endothermic or exothermic peaks are seen due to the slow phase transition (Figure S11).

The full-width-at-half-height (FWHH) of Bragg peaks was used to calculate the coherence length L ("crystal size" using the Scherrer equation. $L_{001} = 52$ nm along [001] direction in the HCP structure of **Au2L** corresponds to ~5.5 unit cells, or 11 layers of NPs. In contrast, L_{111} for the FCC structure of **Au4LC6** along [111] body diagonal, normal to the layers, is 23 nm, corresponding to 4 NP layers.
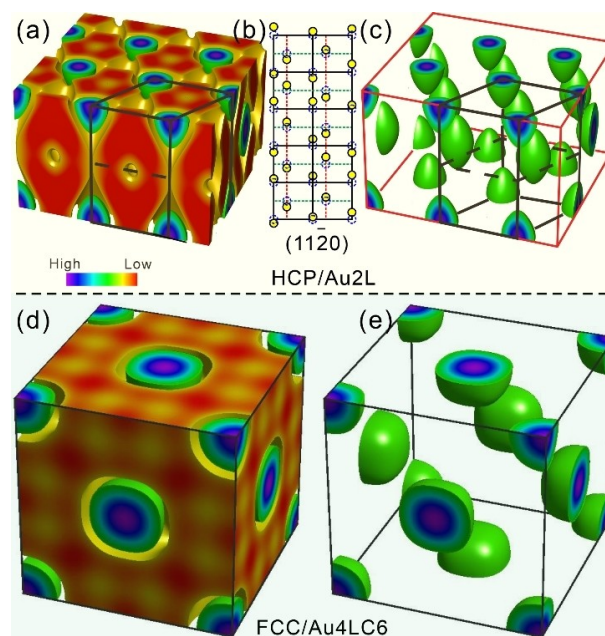
In the ordered phase of both NP systems the scattering at wide angles is diffuse with the maximum corresponding to 0.41 nm correlations, confirming the LC nature. Additionally, a much stronger sharp peak occurs at $q = 26.56$ nm^{-1}, indicating the (111) diffraction of the FCC lattice[12,23] of the gold core (Figure S12).

Thin layers of AuNP systems were also studied by TEM. Dichloromethane solutions were evaporated on carbon film. **Au4LC6** particles are seen to arrange in a monolayer on an

Figure 4. 3D electron density maps of AuNPs reconstructed from SAXS Bragg peak intensities: a), c) HCP phase of **Au2L**, d), e) FCC phase of **Au4LC6**. The colour scale is given on the left. The green isoelectronic surfaces enclose the regions of high electron density (blue-purple), i.e. the AuNPs. In (c) and (e) only the high density regions are shown for clarity. Black lines delineate the unit cell. b) Schematic of the longitudinal positional disorder of the NPs in the HCP giving rise to the ellipsoid shape of the electron density maxima.

Chemistry–A European Journal

Research Article
doi.org/10.1002/chem.202203673

Chemistry Europe
European Chemical
Societies Publishing

The scanned profiles through the maxima in the ED maps, E, are convolutions of the shape of the particle P and the smearing (thermal disorder) function S. Thus in the xy plane $E_{xy} = S_{xy} \otimes P_{xy}$ and along the z-axis $E_z = S_z \otimes P_z$. Approximating all three functions with Gaussians of FWHH s, e and p, we have $e^2 = p^2 + s^2$. Knowing that the diameter of the AuNP is $p = 2.05$ nm and inserting the FWHH values of the appropriate ED peaks e, we get for the principal axes of the deconvoluted "thermal smearing" ellipsoid:

$$s_{xy}^2 = e_{xy}^2 - p_{xy}^2 = 2.25^2 - 2.05^2$$
$$= 0.86 \text{ nm}^2 \quad s_{xy} = 0.93 \text{ nm}$$

$$s_z^2 = e_z^2 - p_z^2 = 3.41^2 - 2.05^2$$
$$= 7.43 \text{ nm}^2 \quad s_z = 2.72 \text{ nm}$$

Thus the standard deviation of the 2.05 nm AuNP from the ideal lattice position in the HCP phase is only $s_{xy}/2 = 0.5$ nm in the xy plane, but is $s_z/2 = 1.4$ nm, that is, three times larger, along z (Figure 4b).

Finally, as with the pure ligand, photoisomerization experiments were conducted. While the UV-vis spectra indicated that isomerization took place, the expected resulting phase change was too slow to be investigated further.

Discussion

To fill space and not leave holes in the structure, the super-lattice must allow ligands to reach points M furthest away, at a distance Λ from the centre of the NPs, or Δ from their surface. Moreover, the flexible ligands should not have to be fully extended to reach M as this would be entropically unfavourable. At the same time, the organic corona should also allow the NPs to approach each other at the closest points in the given lattice, the minimal distance between particle centres being 2λ, and that between their surfaces 2δ.

The two "close-packed" structures, HCP and FCC, have two types s of interstices, regular tetrahedral and regular octahedral. In Figure 5 we show three different views of the HCP and FCC each, with the centres of the tetrahedral and octahedral vacancies shown in green and yellow, respectively, as small tetrahedra and cubes. In Figure 5 the NPs and the unit cells are drawn to scale with the two respective experimental systems in this work, **Au2L** and **Au4LC6**. To reach the furthest point from any NP, the ligand must reach the centre of one of the yellow cubes. Figures 5c, f show crystallographic planes chosen so as to contain the centres of both an octahedral and a tetrahedral interstice, as well as the centres of at least two adjoining NPs. The extended ligands, also shown to scale in Figures 5c, f, are seen to reach the yellow cubes in both structures, but in the
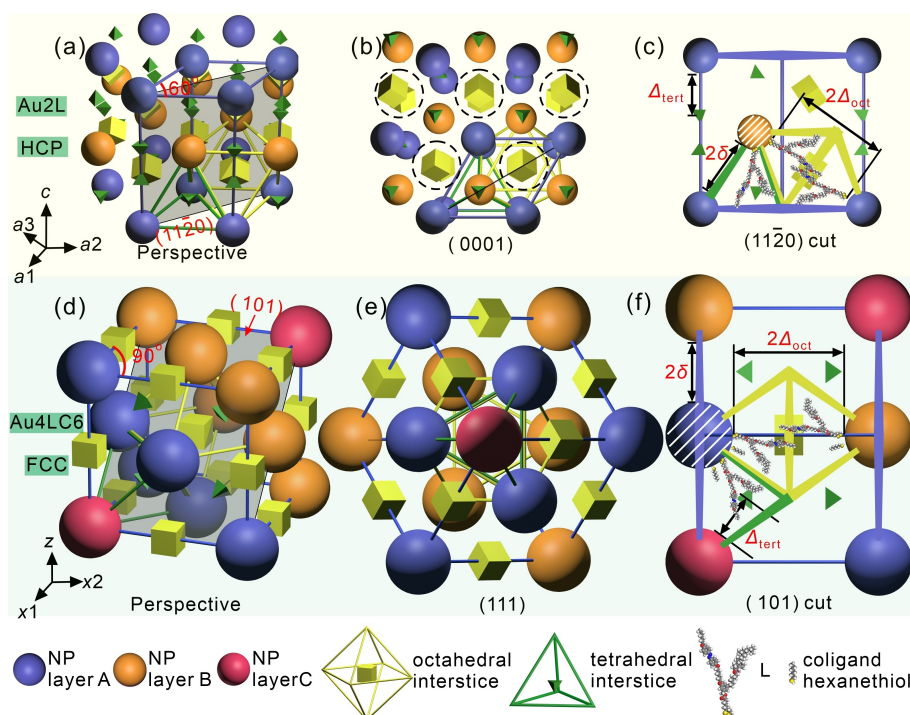

Figure 5. Models of the HCP and FCC structures in the current AuNP systems. a) Perspective view of HCP in **Au2L** showing AuNPs as spheres, and tetrahedral and octahedral interstices as small tetrahedra and cubes. b) As (a) but viewed along the 6_3 screw axis (c-axis, top view) showing the two layers (A,B) of hexagonally packed NPs labelled by different colours; dotted circles indicate the channels along the c-axis. c) View of the $(11\bar{2}0)$ plane of the HCP showing ligands reaching the two selected interstices. d) Perspective view of FCC in **Au4LC6** and e) view along the body diagonal, the $\bar{3}$ axis [111] showing the three densely packed hexagonal layers (A,B,C) of the NPs. f) View of the (101) plane of the FCC showing ligands reaching the two selected interstices, but in the case of the octahedral only just. The lattice planes displayed in (c) and (f) are shown shaded in (a) and (d), respectively. The NPs' diameters and unit cell sizes are to scale with the experimental dimensions for **Au2L** and **Au4LC6**.

Chemistry–A European Journal

Research Article
doi.org/10.1002/chem.202203673

**Chemistry
Europe**
European Chemical
Societies Publishing

FCC phase of **Au4LC6** only just. If the ligand were any shorter, an ordered structure most likely would not have formed.

Geometric requirements that a soft corona must fulfil to allow its hard-core NP to pack on a selection of common lattices are discussed next. Also considered are the necessary conditions for achieving a desired degree of anisotropy promoted by an attached nematogenic ligand. Table 1 contains a list of expressions for Λ and λ, the distances to the furthest point M most difficult to reach, and to the middle of the gap between the two closest NPs, where steric clash is most difficult to avoid. The lattices included are FCC, HCP, BCC and BCT. Note that, while the large interstices in FCC and HCP are regular octahedra with M in their centre, in BCC the octahedra are uniaxially squashed each containing four minimum density points M in the equatorial plane. In a prolate ($c>a$) BCT unit cell obtained by stretching the BCC cell, first the four M points move toward the centre of the octahedron, merging into one when $c/a = \sqrt{2}$ (regular octahedron), then splitting again into two and moving apart along meridional axis as c/a increases further. Hence the two different expressions for Λ and λ in the BCT case. The last column in Table 1 gives the ratio Λ/λ between the longest and shortest distance from NP centre that the corona must be able to accommodate, and Figure 6a plots the dependence of Λ/λ on the c/a ratio of a BCT unit cell.

The plot in Figure 6a starts with the special case of BCC, showing the lowest value of Λ/λ. This reflects the high degree of "sphericity"[24] of the surrounding of a particle that BCC offers, more precisely, the highest isoperimetrc quotient[25] of the cubooctahedral Voronoi cell of a particle in the BCC. Such a nearly spherical environment puts the lowest demand for adaptability on the corona. Unsurprisingly BCC is often found in NP systems without nematogenic ligands, for example, in long linear hydrocarbon or dendron-coated NPs.[17a,f,g,22] These are the cases where no anisotropy is demanded by the ligand and where the corona provides sufficient volume to allow adoption of a non-close-packed lattice like BCC (free volume in hard-sphere packing: BCC 32%, FCC/HCP 26%). These conditions were not met by any of the LC-AuNP systems with forked nematogenic ligands presented in this or in our previous work,[17h] hence no BCC superlattice was observed.
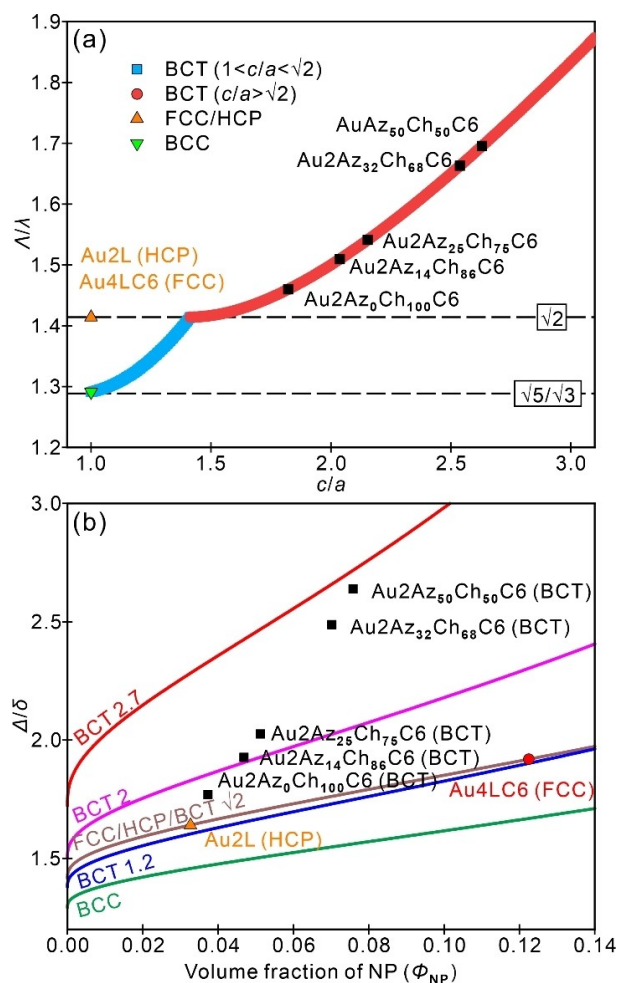
Figure 6. a) Ratio of the longest and shortest distances from the centre of an NP to the surface of its Voronoi cell Λ/λ for BCT structures as a function of the aspect ratio c/a of the unit cell. Red and blue curves correspond to equations for $c/a \geq \sqrt{2}$ and $1 < c/a < \sqrt{2}$ in Table 1. b) Dependence on the volume fraction of the NP metal core of the ratio Δ/δ between the longest and shortest distances from the surface of NP to the surface of its Voronoi cell for BCT with three different c/a ratios and for BCC and HCP/FCC (Table S4). Symbols in black are experimental values for five compounds in ref. [17 h]; those with red labels are from this work.
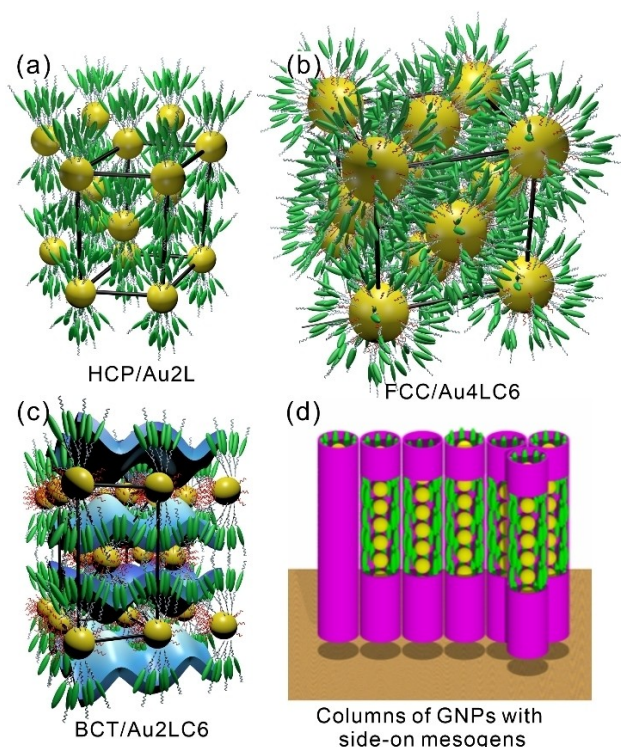
Table 1. Calculated distances from the centre of the nearest NP to the centre of tetrahedral and octahedral interstices.

Phase	Interstice	Λ[a]	λ[b]	Λ/λ[c]
FCC	octahedral	$\frac{a}{2}$	$\frac{\sqrt{2}a}{4}$	$\sqrt{2}$
HCP	octahedral	$\frac{a}{\sqrt{2}}$	$\frac{a}{2}$	$\sqrt{2}$
BCT $c/a \geq \sqrt{2}$	stretched octahedral	$\frac{a^2}{2c} + \frac{c}{4}$	$\frac{a}{2}$	$\frac{2a^2+c^2}{2ac}$
BCT $1 < c/a < \sqrt{2}$	squashed octahedral	$\sqrt{\frac{a^2}{4} + \frac{c^4}{16a^2}}$	$\sqrt{\frac{c^2}{16} + \frac{a^2}{8}}$	$\sqrt{\frac{4a^4+c^4}{2a^4+a^2c^2}}$
BCC	squashed octahedral	$\frac{\sqrt{5}}{4}a$	$\frac{\sqrt{3}}{4}a$	$\frac{\sqrt{5}}{\sqrt{3}}$

[a] $\Lambda=$ distance between most distant point (in FCC and HCP centre of octahedral interstice) and centre of nearest NP. [b] $\lambda=$ half the centre-to-centre distance between two closest NPs. [c] $\Lambda/\lambda=$ ratio between longest and shortest distance from particle centre that the corona must be able to be extended to and compressed to, respectively.

Chemistry–A European Journal

Research Article
doi.org/10.1002/chem.202203673

Chemistry Europe
European Chemical
Societies Publishing

As the BCC unit cell is stretched giving a BCT cell, the Λ/λ ratio, one of the measures of "asphericity" of the NP environment increases, first following the blue curve in Figure 6a then continuing as the red curve, in accord with the two regimes in Table 1. The five points on the red curve mark the positions of the five AuNP systems with forked ligands described in our previous work.[17h] They all contain hexylthiol (**C6**) co-ligands and differ in the molar ratio of azobenzene to cholesterol in their corona, as indicated in their acronyms. All five form the BCT phase whose structure is shown in Figure 7c, with pronounced anisotropy and layering. The rod-like mesogens are contained within the characteristic "egg-box" modulated layers. In Figure 6a, the c/a ratio is seen to increase as the fraction of the thick cholesterol decreases and that of the thinner azobenzene increases, reducing parameter a at constant c. These five compounds were obviously able to provide the anisotropy favoured by their nematogenic ligands, achieving a reasonably high orientational order parameter of the mesogens as shown by their relatively high birefringence and, in **AuAz$_{50}$Ch$_{50}$C6**, plasmonic dichroism. In the current context the question is why the two compounds introduced in this work do not follow the same trend; **Au2L** forms HCP with only weak anisotropy, and **Au4LC6** forms FCC with no anisotropy. The

asphericity of their NP environment is low, with $\Lambda/\lambda = \sqrt{2}$ in both cases.

To explain this behaviour, it is instructive to examine not only Λ and λ, the distances to the furthest and the nearest points on the surface of their NP Voronoi cell from its centre but, more appropriately, the distances from the NP surface, Δ and δ. These latter distances and their ratios are given in Table S4 for all compounds in our current and previous studies. The Δ/δ ratio is a more sensitive measure of asphericity than the Λ/λ. In Figure 6b Δ/δ is plotted against the volume fraction Φ_{NP} of the metal NP core (for volume fraction calculation, see Table S1). The Δ/δ versus Φ_{NP} functions are shown for BCT with the three representative c/a ratios, as well as for BCC and FCC/HCP. They demonstrate vividly the asphericity that the corona must be able to accommodate. The symbols indicate the positions of our seven NP systems in the Δ/δ-Φ_{NP} space. We can see that the two compounds prepared in this work (red symbols) both adopt a structure that demands a lower Δ/δ for their respective Φ_{NP} value than any of the previous five compounds (black symbols). Consider **Au2L**. Its ligand is similar to that in **Au2Az$_{50}$Ch$_{50}$C6**, which shows maximum anisotropy of all our compounds, but requires $\Delta/\delta \sim 2.7$. However, such high adaptability of the corona of **Au2Az$_{50}$Ch$_{50}$C6** seems only possible because of the presence of the **C6** co-ligand, which is absent in **Au2L**. Furthermore, it appears that the only way the co-ligands could help in making the corona sufficiently adaptable is by both the ligands and the co-ligands migrating around the gold NP surface; this way the ligands concentrate in areas requiring a corona thickness Δ, while the co-ligands congregate in areas with corona thickness δ. Whether such ligand migration is possible is still somewhat controversial, but there is indirect evidence, similar to the current case, that supports such mobility at elevated annealing temperatures.[17d,26] Not having co-ligands, **Au2L** is unable to form a highly anisotropic BCT phase and has instead adopted the HCP with a much less demanding Δ/δ value of ~ 1.6.

In contrast to **Au2L**, the 4 nm particles **Au4LC6** do contain the **C6** co-ligand, yet adopt the completely isotropic FCC. Again, inspection of Figure 6b suggests the reason. To achieve a BCT structure with a c/a anisotropy like its 2 nm analogue **Au2Az$_{50}$Ch$_{50}$C6**, the Δ/δ ratio would have a prohibitively high value of ~ 3.5, which its relatively thin corona could not provide. In fact its high volume fraction demands a high value of $\Delta/\delta \sim 2$ even to allow it to form the isotropic FCC.

As seen in Figure 5f, the ligands in **Au4LC6** are just able to reach the centre of the octahedral vacancies, but only if they are extended and oriented directly toward the vacancy centre. This leaves the ligands no freedom to adopt anisotropic nematic-like orientational order, despite the presence of the mobile co-ligand. In contrast, the 2 nm NPs of **Au2L** do possess a degree of anisotropy allowed by their HCP packing, even if they lack a co-ligand. As can be seen from Figure 6b, the significantly lower Φ_{NP} of **Au2L** means a lower Δ/δ of only 1.64, one that its corona is able to adapt to even without help from a co-ligand. As seen in Figure 5c the ligands of **Au2L** are able to reach the centre of octahedral interstices relatively easily, which gives them sufficient freedom to adopt weak nematic-like

Figure 7. Models of mesogen-coated AuNPs. a) Weak preferred orientation of mesogens along the c-axis in the HCP superlattice of **Au2L** with forked ligands but no co-ligands. b) Isotropic distribution of mesogens in the FCC structure of **Au4LC6** with forked ligands and co-ligands. c) BCT structure of 2 nm NP systems **Au2Az$_x$Ch$_{100-x}$C6** in Ref. [17 h]. d) Highly oriented strings of AuNPs with interparticle spacings adjustable by co-ligand fraction jacketed by axially oriented side-on attached rod-like mesogens from Ref. [26b]. Gold: yellow, co-ligands: red, mesogens: green.

Chemistry–A European Journal   Research Article
doi.org/10.1002/chem.202203673

**Chemistry
Europe**
European Chemical
Societies Publishing

anisotropy reflected in the birefringence visible in Figure 2d–f. As has already been noted,[27] HCP structure leaves rows of large octahedral interstices along *c*-axis as channels through which nematic order can propagate without interruption; they are marked with dashed circles in Figure 5b. No such channels exist in FCC, hence there would have been no advantage to **Au4LC6**, which could not develop nematic order anyway, to form HCP and abandon the entropically marginally more stable FCC. As is known, for hard spheres FCC offers a slightly higher translational entropy than HCP by a margin of only 0.001–0.005 k_B per particle (k_B is Boltzmann's constant).[28]

We also wish to add that somewhat longer aliphatic spacers (by 2 or 3 CH_2 groups) in the ligands in our previous paper[17h] may have played an additional role in aiding the pliability of the corona, enabling it to adapt to a higher Δ/δ ratio where required.

It is also worth noting that, using *m*-phenylene benzoate ligand on AuNPs, Lewandowski et al. observed the phase sequence BCT-BCC-FCC upon heating.[17g] The first transition is understandable in terms of the above scheme. As the flexible spacer and tail of the ligand contracted longitudinally, the thinner corona required a smaller Δ/δ ratio, favouring the BCC. The second transition led to a very poorly ordered FCC; it is likely that further shrinkage of the ligands, thinning down the corona to the extent that the NP acted effectively as a hard sphere, choosing the optimal hard sphere packing. It is likely that voids were present in the interstices.

Conclusions

Based on the above results, the requirements for obtaining ordered nanoparticle arrays can be summarized as follows.

- NPs must have a narrow size distribution, particularly if they are large relative to the size of the ligand.
- The corona must be flexible enough to accommodate the difference between Δ and δ (Figure 7b). If anisotropy is not required, then this is achievable by using large flexible ligands such as dendrons. A BCC lattice is most likely to result.
- Preferably use ligands with divergent shape, ideally a square wedge, where the cross-sectional area approximately follows $A \propto R^2$, where R is the distance from NP centre.
- While the above conditions should ensure thermodynamic stability, for kinetic accessibility, the corona should make up a large volume fraction and maximize the amount of conformationally flexible moieties effective in suppressing the glass transition temperature.
- Additional requirements to obtain anisotropic structures with isotropic core NPs are 1) inclusion of a nematogenic rod-like or disk-like unit in the ligand, 2) ensuring a large enough ligand volume, or a low enough volume fraction of the metal core, 3) "dilution" of the mesogenic ligand with shorter flexible co-ligands that would allow a highly aspherical Voronoi cell surrounding the NP, featuring a large Δ/δ quotient (Figure 7c). 4) Weak anisotropy can be achieved even without co-ligands, as exemplified by HCP formation

with compound **Au2L** (Figure 7a). 5) So far the most versatile ligand type for use in anisotrobic NP arrays is side-on attached straight-rod mesogens, combined with relatively small co-ligands (Figure 7d).

The above guiding principles and the geometric analysis should help in the design of future materials and metamaterials based on ordered NP arrays.

Experimental Section

The synthetic strategy for ligand **L** is based on sequential functionalization of the phenol groups of 3,5-dihydroxybenzyl alcohol with the chiral and the photochromic groups separated from the central core by hexyloxy spacers. Esterification with lipoic acid yields ligand **L** (Scheme S1).

Au2L were synthesized by a modified Brust-Schiffrin method.[29] The NPs were purified by more than three successive recrystallizations from toluene and ethanol, followed by size-exclusion chromatography over Biobeads SX1. **Au4LC6** were synthesized by a two-step procedure described earlier.[30] Freshly formed AuNPs were passivated by dodecyl amine. The NPs were subsequently reacted in an exchange reaction with an optimized hexylthiol/**L** mixture (1:2) to achieve the highest possible coverage of the NP surface with ligands. This was followed by repeated recrystallization from toluene and ethanol and purification by size-exclusion chromatography over Bio-Beads SX1 to remove unbound thiols and disulfides.

The mesophase texture was studied using an Olympus BX51-P polarizing optical microscope equipped with a Linkam LTS420E hot stage. Images were recorded with an Olympus DP26 video camera.

Thermogravimetric analysis was performed with a Mettler Toledo TGA/DSC3+ system. The measurements were carried out in the 20–800 °C range with 10 K·min⁻¹ heating rate under nitrogen. DSC thermograms were recorded using a TA-DSC250 (TA Instruments) under nitrogen with 10 K·min⁻¹ heating and cooling rate.

Small/wide angle X-ray scattering (SAXS/WAXS) experiments were conducted at beamline BL16B1 of Shanghai Synchrotron Radiation Facility. Samples were held in borosilicate glass capillaries with 10 μm wall thickness and 1 mm diameter. A modified Linkam hot stage with thermal stability within 0.2 °C was used, with a hole for the capillary drilled through the silver heating block and with mica windows attached to it on each side. Temperature was calibrated by melting point of *n*-alkane $C_{40}H_{82}$ as reference.

TEM was performed using a JEOL JEM–F200 microscope. For TEM imaging, materials were dissolved in DCM, then drop-cast onto carbon film on TEM grids. Fourier transformation of TEM images was performed using MATLAB*.

UV-Vis spectra were recorded on a UV-3600 Plus spectrometer (Shimadzu). Solutions of the ligands were held in standard quartz cuvettes with a 10 mm optical path.

Circular dichroism spectroscopy experiments for LC-AuNPs were performed at beamline B23 of the Diamond Light Source. An intense synchrotron-generated light beam of 0.8 × 1.5 mm² in cross-section was used. The beam was deflected vertically through the sample held horizontally between two quartz glass windows in a Linkam hot stage. Only a very weak CD signal attributed to intrinsic chirality of cholesterol was observed for **Au4LC6** (Figure S13).

Electron density (ED) maps were calculated by inverse Fourier transformation using the standard procedure as described in

Chemistry–A European Journal

Research Article
doi.org/10.1002/chem.202203673

Chemistry
Europe
European Chemical
Societies Publishing

International Tables for Crystallography. Integral intensities of all peaks, listed in Table S2-3, were measured using Gaussian peak fitting. As FCC ($Fm\bar{3}m$) and HCP ($P6_3/mmc$) are centrosymmetric, the phase of each peak could be only 0 or π. For FCC phase of **Au4LC6**, the intensities of (111), (200) and (220) were used to reconstruct the ED maps first. Although this gave $2^3 = 8$ possible phase combinations, in reality there only two possible maps with phase combinations (000) and (00π), shown in Figure S14; the other phase combinations just give a shift of origin or a full ED scale inversion. The phase combination (000) gives the expected volume ratio of high (gold) and low (organic) electron density regions. Subsequently the ED map was refined by including the intensities of two additional weaker reflections, (311) and (400). The ED map with phase combination (0000π) was the final choice, shown in Figure 4d, e. The ED map of HCP phase of **Au2L** was reconstructed in a similar way.

Acknowledgements

Conflict of Interest

There are no conflicts to declare.

Data Availability Statement

The 2D X-ray diffraction patterns (.tif files) in this study are available for download at the figshare database, https://figshare.com/articles/dataset/LC-GNPs_Au4LC6/21591192.

[1] J.-S. Lee, Y.-M. Kim, J.-H. Kwon, H. Shin, B.-H. Sohn, J. Lee, *Adv. Mater.* **2009**, *21*, 178–183.

[2] A. Rizzo, C. Nobile, M. Mazzeo, M. De Giorgi, A. Fiore, L. Carbone, R. Cingolani, L. Manna, G. Gigli, *ACS Nano* **2009**, *3*, 1506–1512.

[3] a) D. Schurig, J. J. Mock, B. J. Justice, S. A. Cummer, J. B. Pendry, A. F. Starr, D. R. Smith, *Science* **2006**, *314*, 977–980; b) C. Rockstuhl, F. Lederer, C. Etrich, T. Pertsch, T. Scharf, *Phys. Rev. Lett.* **2007**, *99*, 017401.

[4] A. Chen, A. E. DePrince III, A. Demortière, A. Joshi-Imre, E. V. Shevchenko, S. K. Gray, U. Welp, V. K. Vlasko-Vlasov, *Small* **2011**, *7*, 2365–2371.

[5] a) B. T. Diroll, K. M. Weigandt, D. Jishkariani, M. Cargnello, R. J. Murphy, L. A. Hough, C. B. Murray, B. Donnio, *Nano Lett.* **2015**, *15*, 8008–8012; b) C. Yi, Y. Yang, B. Liu, J. He, Z. Nie, *Chem. Soc. Rev.* **2020**, *49*, 465–508; c) Y. Gao, Y. Zhou, X. Xu, C. Chen, B. Xiong, J. Zhu, *Small* **2022**, *18*, 2106880.

[6] a) R. L. Whetten, M. N. Shafigullin, J. T. Khoury, T. G. Schaaff, I. Vezmar, M. M. Alvarez, A. Wilkinson, *Acc. Chem. Res.* **1999**, *32*, 397–406; b) L. O. Brown, J. E. Hutchison, *J. Phys. Chem. B* **2001**, *105*, 8911–8916; c) S. I. Stoeva, B. L. V. Prasad, S. Uma, P. K. Stoimenov, V. Zaikovski, C. M. Sorensen, K. J. Klabunde, *J. Phys. Chem. B* **2003**, *107*, 7441–7448.

[7] R. J. Macfarlane, B. Lee, M. R. Jones, N. Harris, G. C. Schatz, C. A. Mirkin, *Science* **2011**, *334*, 204–208.

[8] a) U. Landman, W. D. Luedtke, *Faraday Discuss.* **2004**, *125*, 1–22; b) B. L. V. Prasad, C. M. Sorensen, K. J. Klabunde, *Chem. Soc. Rev.* **2008**, *37*, 1871–1883; c) B. Pansu, C. Goldmann, D. Constantin, M. Imperor-Clerc, J.-F. Sadoc, *Soft Matter* **2021**, *17*, 6461–6469.

[9] a) Z. L. Wang, *Adv. Mater.* **1998**, *10*, 13–30; b) Q. Zhang, J. Xie, J. Liang, J. Y. Lee, *Adv. Funct. Mater.* **2009**, *19*, 1387–1398.

[10] C. Gutiérrez-Wing, P. Santiago, J. A. Ascencio, A. Camacho, M. José-Yacamán, *Appl. Phys. A* **2000**, *71*, 237–243.

[11] B. W. Goodfellow, M. R. Rasch, C. M. Hessel, R. N. Patel, D.-M. Smilgies, B. A. Korgel, *Nano Lett.* **2013**, *13*, 5710–5714.

[12] Q. Zhang, K. Kusada, D. Wu, T. Yamamoto, T. Toriyama, S. Matsumura, S. Kawaguchi, Y. Kubota, H. Kitagawa, *Nat. Commun.* **2018**, *9*, 510.

[13] Z. Fan, X. Huang, Y. Han, M. Bosman, Q. Wang, Y. Zhu, Q. Liu, B. Li, Z. Zeng, J. Wu, W. Shi, S. Li, C. L. Gan, H. Zhang, *Nat. Commun.* **2015**, *6*, 6571.

[14] H. Yao, A. Kuriyama, T. Minami, K. Kimura, *J. Colloid Interface Sci.* **2011**, *354*, 55–60.

[15] K. Bian, H. Schunk, D. Ye, A. Hwang, T. S. Luk, R. Li, Z. Wang, H. Fan, *Nat. Commun.* **2018**, *9*, 2365.

[16] S. Hajiw, B. Pansu, J.-F. Sadoc, *ACS Nano* **2015**, *9*, 8116–8121.

[17] a) B. Donnio, P. García-Vázquez, J. L. Gallani, D. Guillon, E. Terazzi, *Adv. Mater.* **2007**, *19*, 3534–3539; b) M. Wojcik, W. Lewandowski, J. Matraszek, J. Mieczkowski, J. Borysiuk, D. Pociecha, E. Gorecka, *Angew. Chem. Int. Ed.* **2009**, *48*, 5167–5169; *Angew. Chem.* **2009**, *121*, 5269–5271; c) K. Kanie, M. Matsubara, X. Zeng, F. Liu, G. Ungar, H. Nakamura, A. Muramatsu, *J. Am. Chem. Soc.* **2012**, *134*, 808–811; d) W. Lewandowski, M. Wojcik, E. Gorecka, *ChemPhysChem* **2014**, *15*, 1283–1295; e) L. Cseh, X. B. Mang, X. B. Zeng, F. Liu, G. H. Mehl, G. Ungar, G. Siligardil, *J. Am. Chem. Soc.* **2015**, *137*, 12736–12739; f) W. Lewandowski, T. Łojewska, P. Szustakiewicz, J. Mieczkowski, D. Pociecha, *Nanoscale* **2016**, *8*, 2656–2663; g) M. Baginski, A. Pedrazo-Tardajos, T. Altantzis, M. Tupikowska, A. Vetter, E. Tomczyk, R. N. S. Suryadharma, M. Pawlak, A. Andruszkiewicz, E. Gorecka, D. Pociecha, C. Rockstuhl, S. Bals, W. Lewandowski, *ACS Nano* **2021**, *15*, 4916–4926; h) Y.-y. Zhao, Y. Cao, G. Siligardi, G. H. Mehl, F. Liu, G. Ungar, *Chem. Asian J.* **2022**, *17*, e202200167.

[18] X. Mang, X. Zeng, B. Tang, F. Liu, G. Ungar, R. Zhang, L. Cseh, G. H. Mehl, *J. Mater. Chem.* **2012**, *22*, 11101–11106.

[19] H. Peng, L. Yu, G. Chen, Z. Xue, Y. Liao, J. Zhu, X. Xie, I. I. Smalyukh, Y. Wei, *ACS Appl. Mater. Interfaces* **2019**, *11*, 8612–8624.

[20] J. Dintinger, B.-J. Tang, X. Zeng, F. Liu, T. Kienzler, G. H. Mehl, G. Ungar, C. Rockstuhl, T. Scharf, *Adv. Mater.* **2013**, *25*, 1999–2004.

[21] M. Matsubara, W. Stevenson, J. Yabuki, X. Zeng, H. Dong, K. Kojima, S. F. Chichibu, K. Tamada, A. Muramatsu, G. Ungar, K. Kanie, *Chem* **2017**, *2*, 860–876.

[22] M. Baginski, E. Tomczyk, A. Vetter, R. N. S. Suryadharma, C. Rockstuhl, W. Lewandowski, *Chem. Mater.* **2018**, *30*, 8201–8210.

[23] R. L. Whetten, J. T. Khoury, M. M. Alvarez, S. Murthy, I. Vezmar, Z. L. Wang, P. W. Stephens, C. L. Cleveland, W. D. Luedtke, U. Landman, *Adv. Mater.* **1996**, *8*, 428–433.

[24] V. Lucarini, *J. Stat. Phys.* **2009**, *134*, 185–206.

[25] "Isoperimetric Quotient", H. Kremer, E. W. Weisstein from *MathWorld–A Wolfram Web Resource* can be found under https://mathworld.wolfram.com/IsoperimetricQuotient.html, **2022**.

[26] a) A. M. Jackson, J. W. Myerson, F. Stellacci, *Nat. Mater.* **2004**, *3*, 330–336; b) X. B. Zeng, F. Liu, A. G. Fowler, G. Ungar, L. Cseh, G. H. Mehl, J. E. Macdonald, *Adv. Mater.* **2009**, *21*, 1746–1750; c) T. Bürgi, *Nanoscale* **2015**, *7*, 15553–15567.

[27] N. A. Mahynski, A. Z. Panagiotopoulos, D. Meng, S. K. Kumar, *Nat. Commun.* **2014**, *5*, 4472.

[28] a) L. V. Woodcock, *Nature* **1997**, *385*, 141–143; b) P. G. Bolhuis, D. Frenkel, S.-C. Mau, D. A. Huse, *Nature* **1997**, *388*, 235–236; c) S. C. Mau, D. A. Huse, *Phys. Rev. E* **1999**, *59*, 4396–4401.

[29] M. Brust, M. Walker, D. Bethell, D. J. Schiffrin, R. Whyman, *J. Chem. Soc. Chem. Commun.* **1994**, 801–802.

[30] a) R. S. Ingram, M. J. Hostetler, R. W. Murray, *J. Am. Chem. Soc.* **1997**, *119*, 9175–9178; b) Y. Chen, X. Wang, *Mater. Lett.* **2008**, *62*, 2215–2218.

RESEARCH ARTICLE

Gold nanoparticles coated with forked rod-like bimesogen ligands formed two close-packed 3D lattices, HCP and FCC. The former had partially oriented nematic-like mesogens. Geometric analysis of these and other superlattice structures produced rules to help design nanoparticle coronas giving rise to desired isotropic and anisotropic plasmonic superlattices.
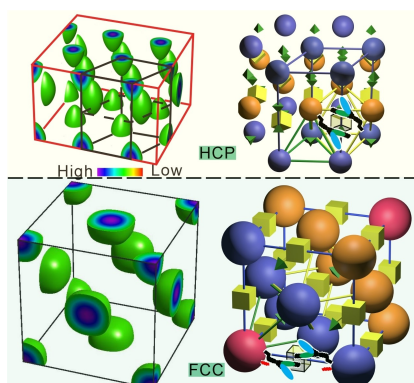
Y.-y. Zhao, Dr. Y. Li, Dr. Y. Cao, Prof. G. H. Mehl*, Prof. F. Liu*, Prof. G. Ungar*

1 – 10

The Effect of Mesogenic Coronas on the Type and Anisotropy of Gold Nanoparticle Superlattices: When Can the Tail Wag the Dog?